BNL-229399-2026-JAAM

pH-Mediated Strong Metal-Support Interaction Construction Through Dynamic Fermi Level Tuning

K. Siniard, X. Tong

To be published in "Angewandte Chemie International Edition"

February 2026

Center for Functional Nanomaterials

Brookhaven National Laboratory

U.S. Department of Energy

USDOE Office of Science (SC), Basic Energy Sciences (BES). Scientific User Facilities (SUF)

DISCLAIMER

pH-Mediated Strong Metal-Support Interaction Construction Through Dynamic Fermi Level Tuning

Kevin M. Siniard,[a] Hailing Yu,[a] Shuai Yuan,[b] Qingju Wang,[a] Xin Wang,[c] Meijia Li,[c] Caiqi Wang,[c] Xiao Tong*,[d] Alexander S. Ivanov,[e] Yuanpeng Zhang,[f] Yongqiang Cheng,[f] Murillo Longo Martins,[f] Tao Wang,[c] Felipe Polo-Garzon,[c] De-en Jiang,[b] Zili Wu,[c] Zhenzhen Yang*,[c] and Sheng Dai*,[a, c]

[a] K. M. Siniard, Dr. H. Yu, Dr. Q. Wang, and Dr. S. Dai
Department of Chemistry, Institute for Advanced Materials and Manufacturing
University of Tennessee, Knoxville
Knoxville, TN, 37996, USA.

[b] S. Yuan, Dr. D. Jiang
Department of Chemical and Biomolecular Engineering
Vanderbilt University
Nashville, TN 37235, USA.

[c] Dr. X. Wang, Dr. M. Li, Dr. C. Wang, Dr. T. Wang, Dr. F. Polo-Garzon, Dr. Z. Wu, Dr. Z. Yang, and Dr. S. Dai
Chemical Sciences Division
Oak Ridge National Laboratory
Oak Ridge, TN, 37831, USA.
Email: yangz3@ornl.gov; dais@ornl.gov

[d] Dr. X. Tong
Center for Functional Nanomaterials
Brookhaven National Laboratory
Upton, NY 11973-5000, USA.
Email: xtong@bnl.gov

[e] Dr. A. Ivanov
Department of Nuclear Engineering
University of Tennessee, Knoxville
Knoxville, TN 37996, USA.

[f] Dr. Y. Zhang, Dr. Y Cheng, Dr. M. Martins
Neutron Scattering Division
Oak Ridge National Laboratory
Oak Ridge, TN 37831, USA.

Supporting information for this article is given via a link at the end of the document.

Abstract: The metal–support interface is central to governing catalytic transformations. While strong metal–support interaction (SMSI) is an established strategy to tailor the morphology and electronic properties of supported metal catalysts, the role of interfacial charge redistribution in SMSI formation remains poorly understood and rarely leveraged. Here, we report a dual-stimuli approach that combines pH modulation with ultrasonication to mediate SMSI construction in aqueous solution through dynamic Fermi level tuning. By leveraging in situ pH-driven charge redistribution at the metal–support interface, we achieve controllable SMSI encapsulation of metal nanoparticles, as verified by electrochemical analysis, work function measurements, and X-ray-based techniques. The resulting catalysts exhibit tunable SMSI features and deliver enhanced activity and selectivity in hydrogenation reactions. This work establishes a facile strategy to modulate catalyst structure and electronic properties by exploiting Fermi level variation as a driving force, thereby advancing rational SMSI design and catalytic performance across diverse environments.

Introduction

The metal–support interface is central to governing catalytic transformations.[1-4] Particularly, strong metal–support interaction (SMSI) construction has emerged as a powerful strategy to tune the performance of heterogeneous catalysts, providing enhanced stability and tunable activity/selectivity through encapsulation of metal nanoparticles (NPs) by their oxide supports.[2, 5-7] Such encapsulation, typically triggered by external stimuli including heat, mechanochemical force, or ultrasonication, suppresses sintering and agglomeration while imparting steric and electronic modulation to metal sites.[8-14] Despite these advances, conventional SMSI construction usually relies on high-temperature reduction (>300 °C under H_2) of reducible oxide supported-metal catalysts.[2, 15] Although the SMSI landscape has expanded with alternative supports (e.g., oxidative metal oxides, boron nitride, carbon, and silica) and lower-temperature techniques such as atomic layer deposition, photoinduction, mechanochemical, and wet-chemical approaches,[9, 16-20] strategies that operate under ambient conditions and enable controllable SMSI formation remain scarce. Addressing this challenge requires a deeper understanding of the fundamental physicochemical factors governing SMSI construction.

Recent theoretical study has shown that metal–metal cohesive interactions can outweigh metal–support bonding in late-transition metal catalysts, highlighting bonding competition as a thermodynamic driver of SMSI construction.[6] In addition, in single-atom catalysts, frontier molecular orbital (FMO) theory has been applied to link the energy levels of metal and oxide support with enhanced activity and stability, particularly the lowest unoccupied molecular orbital (LUMO) of the support.[21] These studies underscore the central role of electronic properties of metal and support in controlling SMSI formation and tuning catalytic behavior. However, the role of in situ charge and electron density redistribution at the metal–support interface during SMSI formation remains poorly understood and rarely leveraged.

To address this gap, we present a dual-stimuli strategy to modulate SMSI construction over supported metal catalysts by harnessing dynamic Fermi level (E_F) tuning in aqueous media of varying pH, leading to enhanced catalysis during subsequent reactions in gas-phase or non-polar media. This approach leverages SMSI construction induced by ultrasonication under ambient conditions, and by adjusting the pH of the aqueous solution, the Fermi level of metal catalysts can be precisely tuned in situ, with lower pH leading to lower in situ Fermi levels and stronger SMSI encapsulation, while higher pH results in the opposite trend. These variations were thoroughly characterized using electrochemical analysis, chemisorption, microscopy, and X-ray-based techniques. Crucially, the pH-mediated SMSI encapsulation greatly affects their catalytic performance. Catalysts treated at lower pH (e.g., pH4) exhibited enhanced activity and selectivity in gas-phase and non-polar liquid-phase hydrogenation of alkynes compared with the pristine catalyst and that from higher pH treatment (e.g., pH10). This work establishes an efficient method to mediate the SMSI construction via in situ Fermi level tuning, enabling sustained catalytic enhancement beyond traditional catalyst modification.

Results and Discussion

Controlling SMSI construction by dynamic Fermi level tuning

As SMSI formation and encapsulation extent are governed by the electronic properties of the metal sites and support, strategies enabling charge and electron density redistribution at metal-support interface can modulate SMSI construction.[22, 23] Motivated by this, we propose a dual-stimuli strategy combining pH variation and ultrasonication with the assumption that 1) proton interactions at the solid–liquid interface, governed by solution pH, modulate catalyst electronic properties by driving spontaneous proton transfer between bulk solution and metal NPs.[24] This alters the formation and deprotonation of surface adsorbed protons (H*), depleting or retaining electrons on the NPs and thereby shifting the E_F;[25, 26] and 2) ultrasonication induces sub-oxide defect formation and Ti^{3+} migration, promoting overlayer encapsulation with the extent governed by E_F and charge redistribution at the metal–support interface.[11, 27] Together, these stimuli enable simultaneous E_F refinement and SMSI construction, providing a viable route to convert transient electronic states into permanent catalytic architectures.

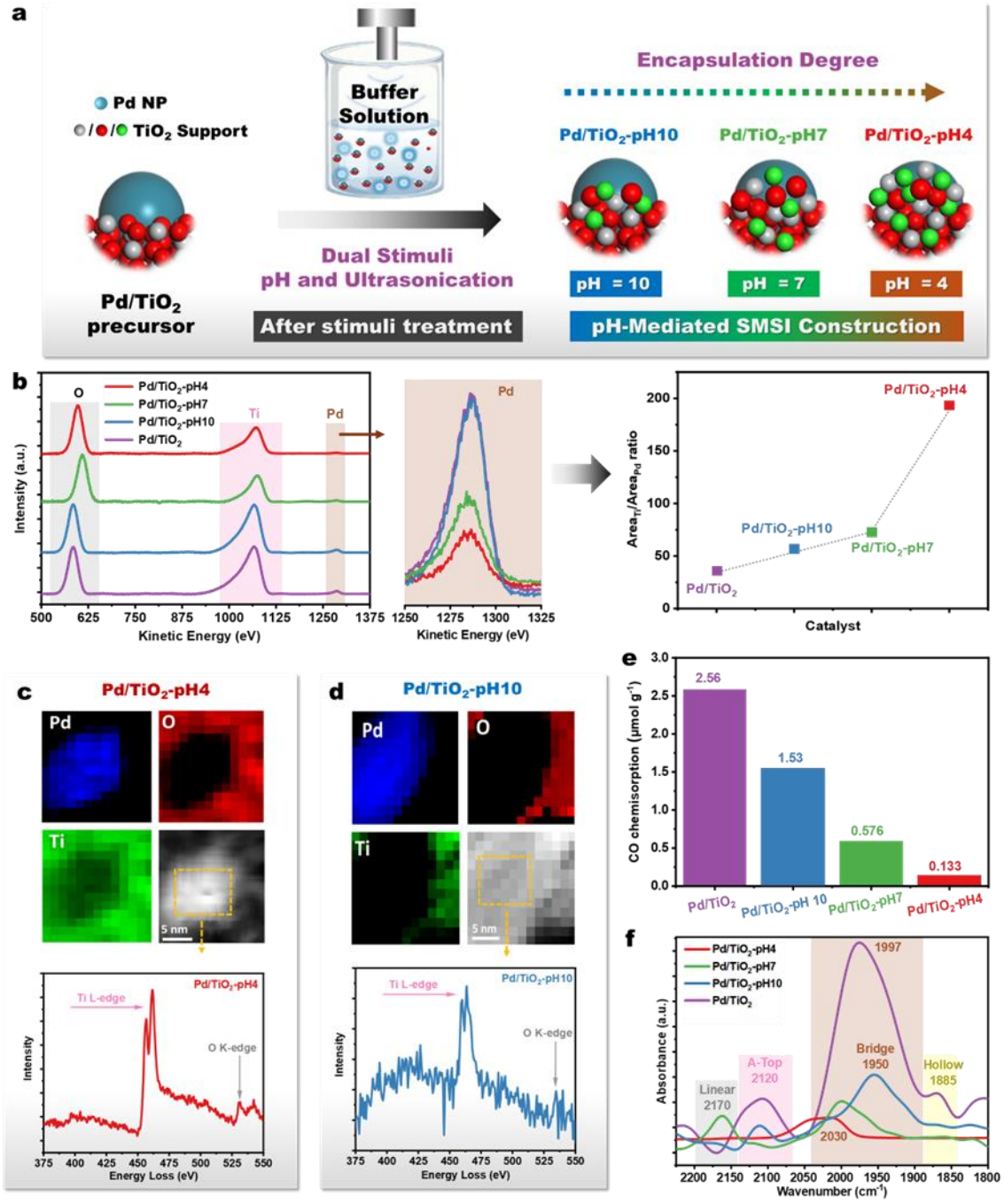

Figure 1 (a) Schematic illustration of SMSI encapsulation assisted by dual external stimuli using pH adjusted aqueous solutions and ultrasonication. (b) LEIS spectra and Ti/Pd LEIS peak area ratio for each catalyst. (c) EELS mapping of Pd/TiO2-pH4 and (d) Pd/TiO2-pH10 featuring Pd, Ti, and O signals with EELS spectra from the orange box region. (e) CO chemisorption and (f) CO DRIFTS results for each catalyst.

The feasibility of controlling SMSI constructions via pH modulation was evaluated using a TiO_2-supported Pd catalyst (Pd/TiO_2), which was then subjected to ultrasonication in Britton–Robinson buffer solutions at pH 4, 7, and 10, yielding catalysts denoted as Pd/TiO_2-pH4, Pd/TiO_2-pH7, and Pd/TiO_2-pH10, respectively (Figure 1a). These conditions were chosen to systematically explore how pH affects E_F modulation and whether the ultrasonication-induced SMSI encapsulation degree can be tuned via pH. The degree of SMSI encapsulation was first assessed by low-energy ion scattering (LEIS) (Figure 1b), which sensitively probes surface composition and an increased Ti/Pd ratio reflects oxide overlayer formation. The LEIS spectra show distinct Pd, Ti, and O signals at 1286, 1071, and 595 eV, respectively. Notably, the Pd signal intensity decreased progressively from Pd/TiO_2-pH10 to Pd/TiO_2-pH4, reflecting diminished surface Pd exposure and enhanced encapsulation at lower pH. This observation was supported by the Ti/Pd peak area ratio, which increased as the pH decreased, confirming greater Ti overlayer coverage of Pd in Pd/TiO_2-pH4. The influence of possible Pd and Ti oxidation or dissolution during ultrasonication was ruled out by the O peak intensity (Figure S1 and Supplementary Note 1) and inductively coupled plasma optical emission spectroscopy (ICP-OES) analysis (Table S1).

Electron energy loss spectroscopy (EELS) mapping of Pd/TiO_2-pH4 (Figure 1c) further confirmed SMSI encapsulation, showing Ti L-edge (456.8 eV) and O signals at the top of Pd NP, which was absent in the pristine Pd/TiO_2 precursor.[11, 28] High-resolution transmission electron microscopy (HR-TEM) images of Pd/TiO_2-pH4 revealed Pd NPs partially covered by TiO_x overlayers, with lattice fringes of 0.23 nm (Pd (111)) and 0.36 nm (TiO_x), and blurred Pd fringes beneath the TiO_x overlayers (Figure S2). Corresponding High-Angle Annular Dark-Field Scanning Transmission Electron Microscopy (HAADF-STEM) images and high resolution energy dispersive X-ray spectroscopy (HR-EDS) mapping of Pd/TiO_2-pH4 also showed Ti and O signals localized on the Pd NPs, whereas the pristine Pd/TiO_2 precursor exhibited no detectable Ti or O signals on or within the Pd NPs, further confirming the existence of SMSI encapsulation on Pd/TiO_2-pH4 and its absence on the Pd/TiO_2 precursor (Figure S3). In contrast, Pd/TiO_2-pH10 displayed weaker and edge-localized Ti L-edge signals, which shifted to higher energy (458.9 eV) (Figure1d), indicating less suboxide overlayer formation. HR-TEM images of Pd/TiO_2-pH10 corroborated these findings, showing only partial encapsulation without discernible TiO_x fringes on top of Pd NP centers (Figure S4 and Supplementary Note 2).

CO chemisorption was employed to probe encapsulation extent on Pd NPs. A systematic decrease in CO uptake with decreasing pH confirmed progressively enhanced SMSI encapsulation (Figure 1e). The untreated Pd/TiO_2 precursor showed a chemisorption value of 2.56 μmol g^{-1}, which decreased to 1.53 μmol g^{-1} (Pd/TiO_2-pH10), 0.58 μmol g^{-1} (Pd/TiO_2-pH7), and 0.13 μmol g^{-1} (Pd/TiO_2-pH4), demonstrating stronger encapsulation at lower pH. CO diffuse reflectance infrared Fourier transform spectroscopy (CO-DRIFTS) analysis further confirmed pH-dependent encapsulation (Figure 1f and Table S2). The untreated Pd/TiO_2 precursor displayed bands at 2120 cm^{-1} (A-top CO on Pd(111) defects)[29], 1997 cm^{-1} (bridge-bonded CO at Pd NP edges)[30], and 1885 cm^{-1} (threefold-hollow CO on Pd(111))[31]. After ultrasonication treatment, Pd/TiO_2-pH10 retained bands at 2120 and 1950 cm^{-1}, Pd/TiO_2-pH7 showed bands at 2170 and 2000 cm^{-1}, while Pd/TiO_2-pH4 exhibited only one band at 2030 cm^{-1}, which can be assigned to linearly adsorbed CO on isolated Pd sites formed after extensive TiO_x coverage. For Pd/TiO_2-pH4, the downward shift from the typical top-site frequency (~2120 cm^{-1}) reflects reduced dipole–dipole coupling among CO adsorbates as Pd ensembles become increasingly isolated under TiO_x overlayer formation, confirming extensive encapsulation.[32] The progressive loss of coordinated CO bands, coupled with reduced band intensity at lower pH (Figure S5), indicates substantial modification of Pd surface sites (Supplementary Note 3). X-ray diffraction (XRD) analysis further supports the controlled SMSI encapsulation following ultrasonication under varying pH conditions (Figure S6), as evidenced by the broadened peak profile and reduced intensity of the Pd (111) reflection, indicative of surface induced amorphization due to TiO_x overlayer formation (Supplementary Note 4).[33] In addition, quantitative analysis of Pd domain sizes derived from extended X-ray absorption fine structure (EXAFS) Pd–Pd coordination numbers (Table S3) shows no systematic dependence on pH and does not correlate with the observed suppression of CO uptake. The modest variation in domain size likely reflects partial amorphization of the Pd surface due to TiO_x overlayer formation, rather than significant nanoparticle fragmentation or growth. Notably, Pd/TiO_2–pH4 exhibits the smallest EXAFS-derived Pd domain size yet displays substantially reduced CO chemisorption, further indicating that Pd nanoparticle size is not the primary factor. Taken together, these results indicate that the pH-dependent reduction in CO uptake arises from SMSI overlayer formation rather than from differences in Pd particle size (Figure S7).

To demonstrate the broader applicability of this pH-modulated SMSI strategy, the same approach was applied to Pt/TiO_2, Pd/ZnO, and Pd/CeO_2, which resulted in analogous trends in metal NP encapsulation as evidenced by diminished XRD peak intensity and reduced CO chemisorption (Figures S8-10 and Supplementary Notes 5-7). For further comparison, classical SMSI was induced by H_2 reduction of Pd/TiO_2 for 2 hr in 5% H_2/He at 300, 400 and 500 °C respectively. XRD shows progressive decrease of the Pd (111) reflection plane with increasing reduction temperature, while CO-DRIFTS reveals rapid suppression and eventual disappearance of Pd–CO bands at 500 °C,

indicating extensive and poorly tunable encapsulation (Figure S11). This is in stark contrast to the pH-modulated strategy where the thermal H_2 SMSI treatment proceeds without fine control over encapsulation extent or interfacial electronic structure.

Valence and structure variation upon pH-driven SMSI encapsulation

To probe defect and suboxide species formation accompanying SMSI construction, the oxidation states of Pd and Ti were analyzed by X-ray photoelectron spectroscopy (XPS). The Pd 3d XPS spectra exhibited a pH-dependent shift to lower binding energies, reflecting increased electron density on Pd after ultrasonication in lower pH (Figures S12-13) indicative of enhanced metal–support electron interaction and partial reduction of Pd species under SMSI conditions.[34] Correspondingly, the Ti 2p XPS peak shifted from 459.0 eV (Ti^{4+} in TiO_2 precursor) to 458.5 eV in Pd/TiO_2-pH4, consistent with TiO_x suboxide overlayer formation and electron-enriched Ti species (Figure 2a). Notably, the Ti 2p binding energy shift correlated linearly with pH of the buffer solution (Figure 2b), underscoring progressively enhanced electron density of the TiO_x overlayer after ultrasonication in lower pH. To distinguish surface-localized electronic effects from changes in the bulk Pd oxidation state, Pd K-edge X-ray absorption near-edge structure (XANES) spectroscopy was performed. Linear combination fitting using Pd foil and PdO references revealed no significant change in the bulk Pd^0/Pd^{2+} ratio across all pH conditions (Figure S14 and Table S4), indicating that ultrasonication-induced SMSI does not result in bulk Pd reduction or oxidation. Moreover, comparison of the normalized Pd K-edge XANES spectra (Figure S15) shows that the pH-treated catalysts exhibit a systematic shift of the pre-edge feature to lower energy, together with an increase in white-line intensity with decreasing pH, which is consistent with enhanced Pd–support orbital hybridization, increased electronic screening at Pd, and reduced Pd–Pd coordination arising from strengthened metal–support interactions rather than bulk PdO formation.[35]

Pd K-edge EXAFS fitting analysis was conducted to examine the local structural environment of Pd (Table S5 and Figure S16). All Pd/TiO_2 samples show lower EXAFS amplitudes (S_0^2) compared with Pd foil, indicating Pd–support interactions, with Pd/TiO_2-pH4 exhibiting the lowest amplitude, consistent with the strongest SMSI encapsulation.[36] Coordination numbers (CN) decreased for Pd/TiO_2-pH4 (10.29) relative to the untreated Pd/TiO_2 precursor (10.77) and slightly increased at higher pH Pd/TiO_2 precursor (Pd/TiO_2-pH7: 10.92 and Pd/TiO_2-pH10: 10.79), confirming that SMSI strength increases under more acidic conditions. Pd–Pd bond distances (ΔR) in the Pd/TiO_2-pH SMSI samples are slightly expanded (~2.49 Å) relative to Pd foil (2.43 Å), suggesting subtle lattice expansion or strain induced by the Pd–support interactions, while Debye–Waller factors (σ^2) remain comparable across all samples, indicating preserved structural integrity.[8] Notably, no Pd–O contributions (~1.38 Å) are observed, confirming that Pd NPs remain predominantly metallic across all pH treatments (Figure S17). These EXAFS results demonstrate that ultrasonication in pH buffers promotes pH-dependent SMSI formation without altering the structural integrity of the Pd NPs, consistent with trends observed in XRD, CO chemisorption and CO-DRIFTS measurements.

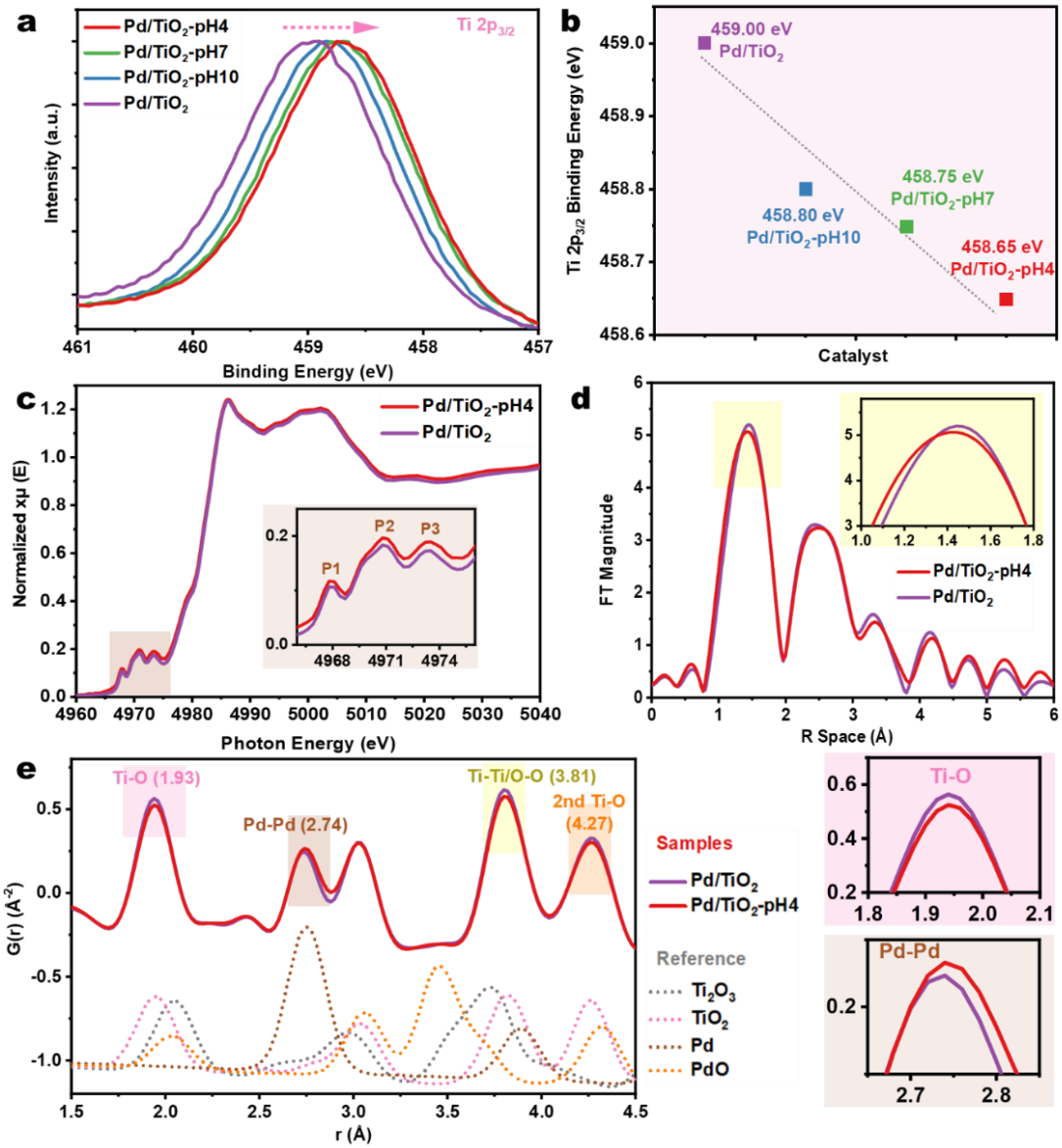

Figure 2 (a) Ti $2p_{3/2}$ XPS spectra of each catalyst. (b) Relationship between Ti $2p_{3/2}$ binding energy shift and solution pH used during ultrasonication. (c) XANES spectra at the Ti K-edge of Pd/TiO_2 and Pd/TiO_2-pH4. (d) FT-EXAFS k3-weighted χ(k) data. (e) Short range atomic PDF spectra.

X-ray absorption fine structure (XAFS) spectroscopy was used to further probe the local coordination and electronic environment of Ti in Pd/TiO_2 and Pd/TiO_2–pH4. In the XANES spectra (Figure 2c), the pre-edge region was deconvoluted into three main features (P1–P3), assigned to excitonic transitions and the quadrupole-allowed 1s → 3d transition.[37] Compared to Pd/TiO_2, Pd/TiO_2–pH4 showed a notable increase in pre-edge intensities without energy shifts, indicating enhanced 3d–4p hybridization and increased local TiO_6 symmetry, approaching rutile-like character while retaining the major anatase phase.[38] The more symmetric local environment may facilitate orbital overlap and charge transfer at the metal–support interface, promoting SMSI overlayer formation.[39] Fourier-transformed extended X-ray absorption fine structure (FT-EXAFS) analysis at the Ti K-edge (Figure 2d) revealed two main coordination shells. The Ti–O path shortened from ~1.47 Å in Pd/TiO_2 to ~1.40 Å in Pd/TiO_2–pH4, while the Ti–Ti path elongated from ~2.42 Å to ~2.48 Å, consistent with defect generation, partial reduction, and structural evolution toward a more uniform TiO_6 environment.[38] FT-EXAFS fitting with an anatase-based model (Figures S18–S19 and Table S6) showed a reduced Debye–Waller factor (σ^2) and positive path length variation (δr) for Ti–O in Pd/TiO_2–pH4, indicating decreased static disorder and convergence of Ti–O bond lengths. The inclusion of third cumulants revealed non-Gaussian local distortions, confirming that while Pd/TiO_2–pH4 possesses a more symmetric local structure, it remains subtly distorted.[40] Collectively, these results demonstrate

that pH-modulated ultrasonication enhances TiO_6 symmetry and local orbital interactions, enabling stronger SMSI overlayer formation.

Synchrotron X-ray pair distribution function (PDF) analysis further probed the local atomic structure of Pd/TiO_2 and Pd/TiO_2-pH4 in real space (Figure 2e). The first coordination shell at 1.93 Å (Ti–O), the correlation at 3.81 Å (Ti-Ti/O-O), and the second-shell Ti-O peak at 4.27 Å showed reduced intensity in Pd/TiO_2-pH4, which may indicate smaller coordination number, oxygen vacancy formation, and electronically enriched Ti species, though the observed difference is small.[41] However, the Pd–Pd correlation peak increased, corroborating XPS evidence of increased electron density around Pd (Figures S12–S13). Longer Pd-related bond distances in Pd/TiO_2-pH4 imply Pd–Ti interactions during SMSI construction.[42] Despite increased disorder, XANES and FT-EXAFS indicate a more symmetric and electronically hybridized local Ti–O environment, lowering surface energy and enhancing orbital overlap at the metal–support interface. These local structural reorganizations provide a foundation for SMSI overlayer formation and interfacial charge redistribution.[38, 43]

Mechanistic insights into dynamic Fermi level tuning during SMSI construction

Previous studies revealed that SMSI encapsulation arises from oxygen vacancies (O_{vac}) and reduced metal cations (e.g., Ti^{3+}) in oxide supports under reductive conditions.[2, 42, 44-46] Accordingly, external stimuli that enrich O_{vac} and reduced metal species ($M^{\delta+}$) are preferred to promote stronger encapsulation. To experimentally probe how pH modifies these surface properties, we performed Mott–Schottky (MS) analysis at 1000 Hz.[47] Specifically, the flat-band potential (V_{fb}), corresponding to E_F alignment with the Ag/AgCl reference electrode, was extracted from MS plots (Figure 3a) and converted to E_F on the vacuum scale (Supplementary Note 8). The resulting E_F values were –3.56, –3.41, and –3.27 eV for pH 4, 7, and 10, respectively, showing a linear correlation across 1500 – 500 Hz (Figures S20–S21). These pH-dependent values reflect the equilibrated electronic state of the Pd/TiO_2 interface, indicating whether the Pd/TiO_2 surface is electron-deficient or electron-rich, and thus provides a mechanistic basis for how pH influences charge redistribution at the Pd/TiO_2 interface.[48] For instance, a more negative shifted V_{fb} (e.g. –1.38 eV (pH 10)) is indicative of Ti-O^- species, while a more positive shifted V_{fb} (e.g –1.08 V (pH 4)) is indicative of Ti-OH_2^+ species.[49] In particular, it is the protonation/deprotonation of surface –OH groups and interfacial dipoles, that shifts the E_F relative to the intrinsic vacuum-level E_F of TiO_2 (–5.15 to –4.7 eV, depending on phase, Pd size, and defect density), thereby modulating the electron density of Pd NPs at the interface.[24]

Previous work has established that SMSI formation is governed by the difference in E_F between the support and the metal ($E_F TiO_2$ > $E_F$metal), which drives migration of reduced species and overlayer formation.[45] Accordingly, modifying the E_F of Pd/TiO_2 via pH shifts the equilibrated E_F at the interface of Pd and TiO_2 (Figure 3a). Thus, the pH-driven E_F modulation governs SMSI formation through distinct interfacial processes (Figure 3b). At pH 4, surface hydroxyls on TiO_2 are protonated ($–OH_2^+$), while Pd NPs undergo protonation (H^*_{ads}), depleting their electron density (e^-_{Pd}) and generating electron-deficient Pd surfaces.[50] The combined effect produces a positively polarized Pd/TiO_2 interface with a lower E_F, which facilitates oxygen vacancy generation and Ti^{4+} reduction to Ti^{3+}. These Ti^{3+} species are then electrostatically attracted to the electron-deficient Pd (satisfying the SMSI formation requirement of $E_F TiO_2$ > $E_F$metal), thereby driving their migration and subsequent SMSI overlayer formation. By contrast, at pH 10, deprotonation by hydroxide anions yields $O^{\delta-}$-enriched TiO_2 and electron-rich Pd NPs, resulting in a higher E_F that suppresses Ti^{3+} migration (Figure 3b). Meanwhile, ultrasonication generates abundant H· radicals, which under acidic conditions accelerate TiO_2 reduction, but under alkaline conditions are consumed by OH^- to form non-reductive species (H_2O_2, $\cdot O^-$), thereby limiting radical-driven reduction.[51, 52] Together, these coupled effects demonstrate how pH simultaneously modulates the E_F and radical chemistry, thereby dictating the extent of SMSI encapsulation. Ultimately ,these results indicate that the observed E_F shifts are not merely descriptors of interfacial electronic states but actively govern SMSI formation by controlling Ti^{3+} migration, oxygen vacancy formation, and Pd–support interactions under different pH conditions.

Secondary electron cutoff spectra further reveal that SMSI formation alters both catalyst geometry and electronic properties (Figure 3c–3d). Upon SMSI construction, the work function (Φ), which is inversely related to the E_F ($\Phi = E_{Vac} – E_F$), of catalysts decreases systematically with decreasing pH, with 4.88 eV (Pd/TiO_2), 4.67 eV (Pd/TiO_2-pH10), 4.12 eV (Pd/TiO_2-pH7), and 4.05 eV (Pd/TiO_2-pH4) demonstrating that SMSI formed under more acidic conditions leads to the most pronounced electronic modulation. Notably, Pd/TiO_2-pH4 exhibits the lowest Φ, consistent with enhanced electron transfer (via migration of reduced $Ti^{\delta+}$) to Pd during encapsulation. These results establish solution pH as a powerful lever to control SMSI extent and interfacial charge transfer.

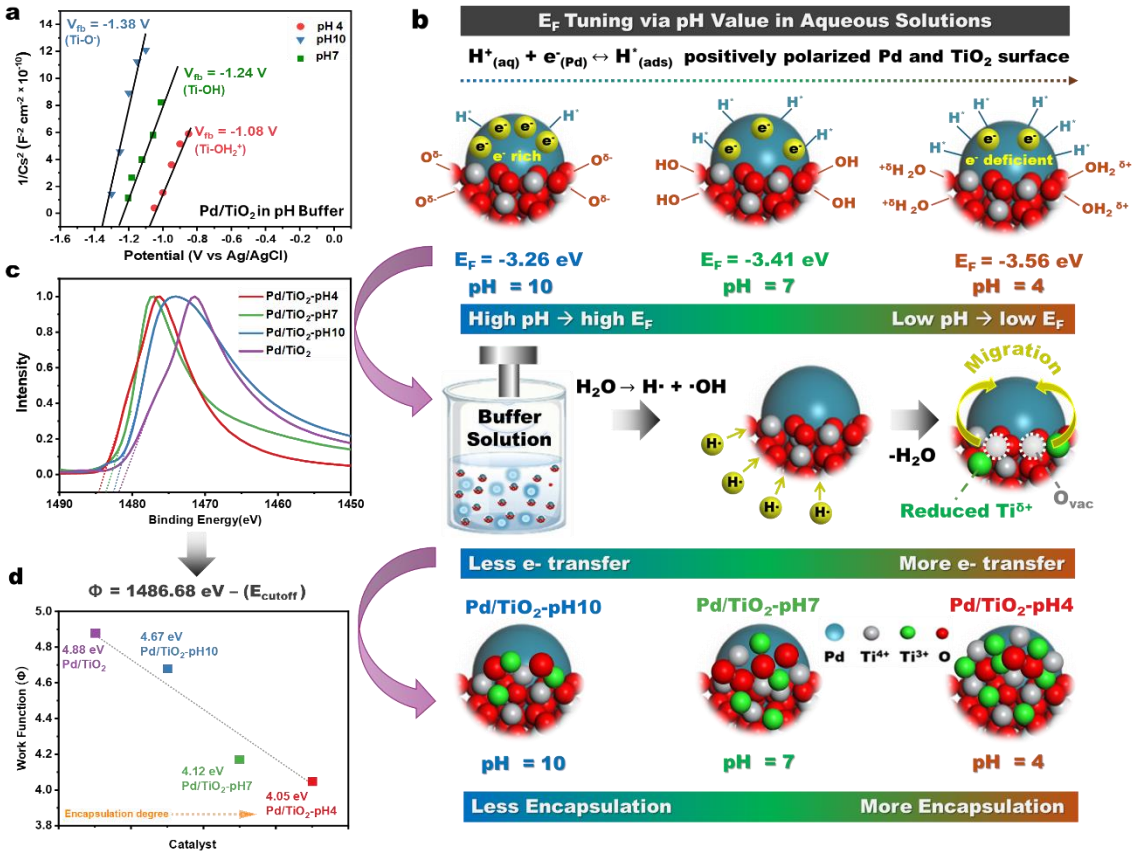

Figure 3 (a) Mott-Schottky plots of Pd/TiO2 in different pH solution and the corresponding protonation and deprotonation states of the TiO2 surface. (b) Schematic illustration of pH-modified SMSI construction through in situ Fermi level tuning. (c) XPS secondary electron cutoff and (d) as-calculated work function of Pd/TiO2 precursor, Pd/TiO2-pH10, Pd/TiO2-pH7, and Pd/TiO2-pH4.

Catalytic enhancement via pH-driven SMSI encapsulation

As demonstrated above, the dual stimuli approach using pH modulation and ultrasonication was used to systematically restructure Pd/TiO2, enabling tunable SMSI encapsulation and associated electronic modulation, ultimately modifying adsorption geometries and binding strength of substrates and intermediates to alter activity and selectivity.[2, 53] The catalysts were evaluated in the gas-phase semi-hydrogenation of acetylene, a probe reaction to assess how electronic and structural modifications stabilized under aqueous conditions influence catalytic behavior. This transformation is industrially critical for purifying ethylene-rich streams used as polymer feedstocks.[54, 55] The key challenge lies in achieving high ethylene selectivity while suppressing over-hydrogenation to ethane, as both species are reactive under hydrogenation conditions.[56, 57] Effective catalysts must deliver near complete acetylene conversion with minimal ethylene loss, while avoiding side reactions such as oligomerization and carbon deposition that compromise stability.[56, 57] Thus, precise control of surface electronic structure and adsorption energetics is essential to enhance both catalytic performance and durability in this process. After screening reaction parameters (Figure S22), 50 °C was selected to evaluate the catalysts upon SMSI construction (Supplementary Note 9). While comparable acetylene conversions were observed: 76% (Pd/TiO2-pH4), 83% (Pd/TiO2-pH7), and 81% (Pd/TiO2-pH10) (Figure 4a), ethylene selectivity varied sharply with encapsulation degree, reaching 88% for Pd/TiO2-pH4 versus 16% for Pd/TiO2-pH10 (Figure 4b). Notably, the low-selectivity regime towards ethylene is consistent with the behavior of the bare Pd/TiO2 catalyst (Figure S23), which are well known to favor over-hydrogenation to ethane due to contiguous Pd ensembles.[58-60] Pd/TiO2-pH4 delivered the highest turnover frequency (TOF) (90.5 s^{-1}), outperforming Pd/TiO2-pH7 (31.3 s^{-1}), and Pd/TiO2-pH10 (19.4 s^{-1}) (Figure

S24). H_2 pulse titration revealed an inverse correlation between exposed Pd sites (Pd/TiO_2-pH10 > Pd/TiO_2-pH7 > Pd/TiO_2-pH4) and encapsulation degree despite comparable Pd loadings and particle sizes (Figure S25). Apparent activation energies (E_a) extracted from Arrhenius plots (Figure S26–S29) confirmed this trend, with Pd/TiO_2-pH4 showing the lowest E_a (29.1 ± 4 kJ mol^{-1}) compared to Pd/TiO_2-pH7 (35.9 ± 3 kJ mol^{-1}) and Pd/TiO_2-pH10 (38.5 ± 3 kJ mol^{-1}). These results establish a linear correlation between catalytic activity and encapsulation extent (Figure 4b), where higher encapsulation (Pd/TiO_2-pH4) corresponds to greater efficiency and lower Ea. Furthermore, the stability of Pd/TiO_2-pH4 was evaluated under acetylene hydrogenation at 50 °C with the same catalyst loading and gas composition as the results shown in Figure 4a. The catalyst maintained conversions between 80–90% with ethylene selectivity of 97-99% over 65 hours. CO DRIFTS along with CO chemisorption showed no significant change in the availability of surface Pd sites, and post-reaction XRD analysis confirmed that the Pd (111) plane peak intensity remained unchanged, indicating negligible sintering and preservation of the SMSI overlayer (Figure S30). These results demonstrate that the encapsulation structure and enhanced activity are maintained under prolonged reaction conditions. Moreover, to rule out contributions from buffer-derived species (e.g. phosphoric and boric acids), XPS and EDS spectra of Pd/TiO_2-pH4 showed no detectable phosphorus or boron species on the catalyst surface (P 2p, ~133–134 eV; B 1s, ~187-193 eV), confirming that the observed catalytic behavior is driven by pH-modulated SMSI formation rather than adsorption and active site coverage from the phosphoric or boric acid species present in the Britton–Robinson buffer (Figure S31).

Beyond gas-phase reactions, the enhanced performance of the treated catalysts was further demonstrated in non-aqueous liquid-phase reactions, using phenylacetylene hydrogenation as a probe reaction (Figure 4c). Under identical reaction conditions at 125 °C, the SMSI modified catalysts achieved comparable phenylacetylene conversions of 72% (Pd/TiO_2-pH4), 80% (Pd/TiO_2-pH7), and 76% (Pd/TiO_2-pH10) (Figure 4c). Similar to the gas-phase results, Pd/TiO_2-pH4 exhibited the highest selectivity toward styrene at 92%. This selectivity trend correlated with the encapsulation degree, with Pd/TiO_2-pH10 showing the lowest styrene selectivity (14.6%) (Figure 4c). For comparison, bare Pd/TiO_2 exhibited similarly low styrene selectivity (Figure S32), consistent with its well-documented tendency to promote over-hydrogenation to ethylbenzene due to extended Pd ensembles.[61] Consistent with gas-phase hydrogenation, Pd/TiO_2-pH4, possessing the lowest Φ after SMSI construction, also demonstrated the highest TOF of 6.2 s^{-1} (Figure S33). Additionally, the number of exposed Pd sites correlated inversely with the encapsulation degree and the catalytic activity (TOF), decreasing in the order: Pd/TiO_2-pH10 > Pd/TiO_2-pH7 > Pd/TiO_2-pH4 (Figure S34). Notably, the Ea for Pd/TiO_2-pH4 was slightly lower at 26.5 ± 3 kJ mol^{-1}, compared to Pd/TiO_2-pH7 (27.4 ± 2 kJ mol^{-1}) and Pd/TiO_2-pH10 (31.8 ± 3 kJ mol kJ mol^{-1}) (Figures S35-S38), confirming the catalytic enhancement achieved through pH-induced Fermi level modulation (Figure 4d). The consistent trends observed in both gas-phase and non-aqueous liquid-phase hydrogenation reactions suggest that the E_F tuning induced by pH adjustment during ultrasonication is not merely a transient effect but a driving force for controllable SMSI encapsulation.

For comparison, classical SMSI was induced by H_2 reduction of Pd/TiO_2 for 2 hr in 5% H_2/He at 300, 400, and 500 °C respectively and evaluated in phenylacetylene hydrogenation. Even though high-temperature reduction similarly attenuated Pd (111) diffraction intensity and suppressed CO adsorption, excessive encapsulation at 500 °C resulted in a pronounced loss of catalytic activity, underscoring the limited tunability of thermally induced SMSI (Figure S39). In contrast, pH-driven SMSI enables controlled SMSI overlayer formation that preserves activity while enhancing selectivity thus demonstrating the viability of pH-driven electronic tuning as a means to modulate SMSI encapsulation.

To first assess whether hydrogen activation contributes to this enhanced catalytic behavior, H_2-D_2 exchange experiments were conducted as a probe of H_2 dissociation and metallic Pd ensemble availability. Notably, Pd/TiO_2-pH4 exhibited a lower HD formation rate relative to the other catalysts (Figure S40), indicating that the enhanced activity does not originate from accelerated H_2 dissociation or increased exposure of metallic Pd sites. This observation instead points to altered surface chemistry and reaction pathways as the dominant contributors to catalytic enhancement, motivating a detailed examination of surface-bound species and interfacial structure. Inelastic neutron scattering (INS) spectra revealed that ultrasonication subtly modified surface-bound water and hydroxyl groups in Pd/TiO_2 catalysts, with fewer confined water molecules and slightly more hydroxyl species in Pd/TiO_2-pH4 (Figure S41). These changes are consistent with the formation of Ti^{3+}/TiO_x species under low-pH conditions, which increase surface hydrophobicity, displace water from the Pd surface, and facilitate the development of a partial SMSI overlayer (Supplementary Note 10).[62] O 1s XPS analysis support the INS results showing more hydroxyl species in Pd/TiO_2-pH4 (Figure S42). Additionally, in situ DRIFTS under acetylene hydrogen conditions (Figure S43) revealed that the enhanced ethylene selectivity of Pd/TiO_2-pH4 arises from π-stabilization of the C=C bond in ethylene without indication of further C-H stretching modes that arise from sigma-bonded ethylene, which is a precursor for hydrogenation to ethane (Table S7).[63] Thus, these changes in surface hydroxyl speciation provide an important link between pH-mediated SMSI construction and catalytic selectivity.

Together, O 1s XPS and INS indicate that Pd/TiO_2-pH4 possesses a surface enriched in hydroxyl groups but is depleted in physisorbed water, consistent with Ti^{3+}/TiO_x formation and increased surface hydrophobicity (Supplementary Note 10). This altered hydroxyl environment suppresses hydrogen transfer mediated by surface –OH/water networks and, together with SMSI-induced site isolation, favors π-bound adsorption of ethylene over σ-bound intermediates, thereby inhibiting over-hydrogenation and enhancing ethylene selectivity (Supplementary Note 11).[63]

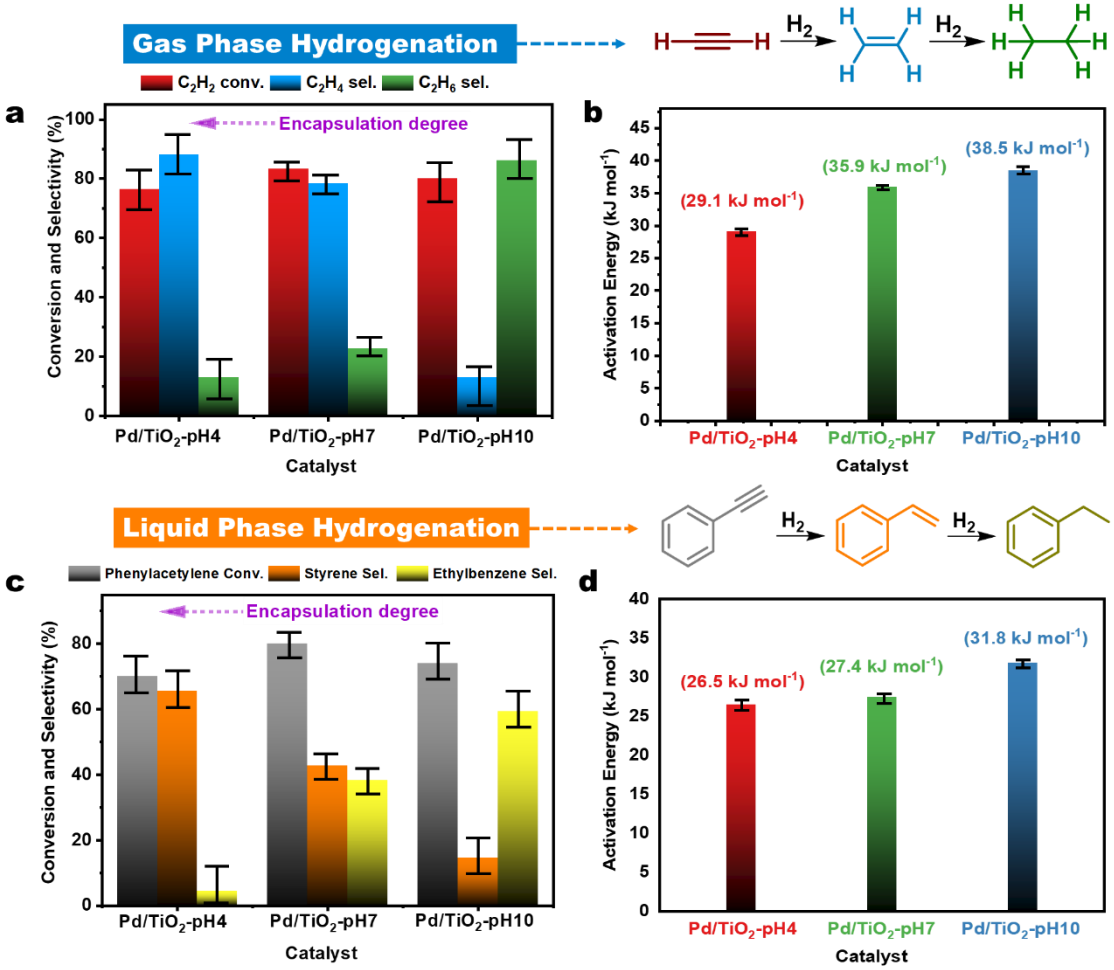

Figure 4 (a) Catalytic performance in acetylene semihydrogenation. Reaction conditions: 0.5% acetylene, 2.5% H_2, 97% argon gas mixture, flowrate 50 ml min^{-1}, catalyst 5 mg, diluted with quartz 50mg, and reaction temperature 50 °C. (b) The E_a of acetylene hydrogenation for each catalyst. (c) Catalytic performance in phenylacetylene hydrogenation. Reaction conditions: 5 mmol phenylacetylene, 0.5 MPa H_2, catalyst 10 mg, reaction temperature 125 °C, and reaction time 1h. (d) The E_a of phenylacetylene hydrogenation for each catalyst.

Theoretical elucidation of enhanced SMSI encapsulation and reaction pathway

Density functional theory (DFT) calculations were performed to investigate the relationship between the encapsulation extent and work function (Φ) of resulting Pd/TiO_2 catalysts and the influence of SMSI encapsulation on the acetylene semihydrogenation pathway. A Pd_{13} cluster partially covered by a reduced TiO_x overlayer (x = 1.5) was used to model varying encapsulation degrees (0%, 50%, 100%, and 150%) (Figure 5a). As the coverage increased from 0% to 150%, the calculated Φ decreased from 4.77 to 4.19 eV (Figure 5b), consistent with experimental Φ values derived from XPS E_{cutoff} of catalysts treated in different pH solutions (Figure 3c–3d). This progressive decrease in Φ reflects that pH-modulated SMSI systematically reshapes the electronic structure of Pd/TiO_2 catalyst and directly governs its catalytic properties. To probe the role of TiO_x overlayer encapsulation on acetylene hydrogenation, full DFT pathway calculations were performed for 0% and 150% $TiO_{1.5}$ coverage, representing bare Pd/TiO_2 and highly encapsulated Pd/TiO_2 catalyst with a few monolayers of $TiO_{1.5}$, respectively. For bare Pd/TiO_2 (0% coverage), the barriers for absorbed ethylene (C_2H_3 → C_2H_4, 0.82 eV) and absorbed ethane (C_2H_5 → C_2H_6, 0.80 eV) formation are nearly identical, with the rate-determining step (RDS) residing in ethylene formation and negligible kinetic distinction between the two products (Figure 5c). In contrast, Pd/TiO_2 (150%

coverage) exhibits markedly altered energetics. While $C_2H_2 \rightarrow C_2H_3$ remains moderately activated (0.66 eV), ethylene formation ($C_2H_2 \rightarrow C_2H_4$) proceeds with a very low barrier (0.20 eV). The RDS shifts to ethane formation ($C_2H_4 \rightarrow C2H6$, 0.94 eV), rendering further hydrogenation kinetically unfavorable and stabilizing ethylene as the dominant product. The full computed energy profiles are presented in Figure 5d, with transition-state structures shown in Figures S44–S45. DFT calculations are consistent with the experimental trends. Over the 150% $TiO_{1.5}$ coverage catalyst, ethylene forms via a low-barrier pathway (0.20 eV), lowering the apparent E_a, while bare Pd/TiO_2 shows higher and comparable barriers for ethylene and ethane formation (0.82 and 0.80 eV, respectively), resulting in poor selectivity. These results demonstrate that pH-mediated SMSI construction enhances TiO_x encapsulation, reshaping the potential energy surface of catalyst to favor selective ethylene formation.

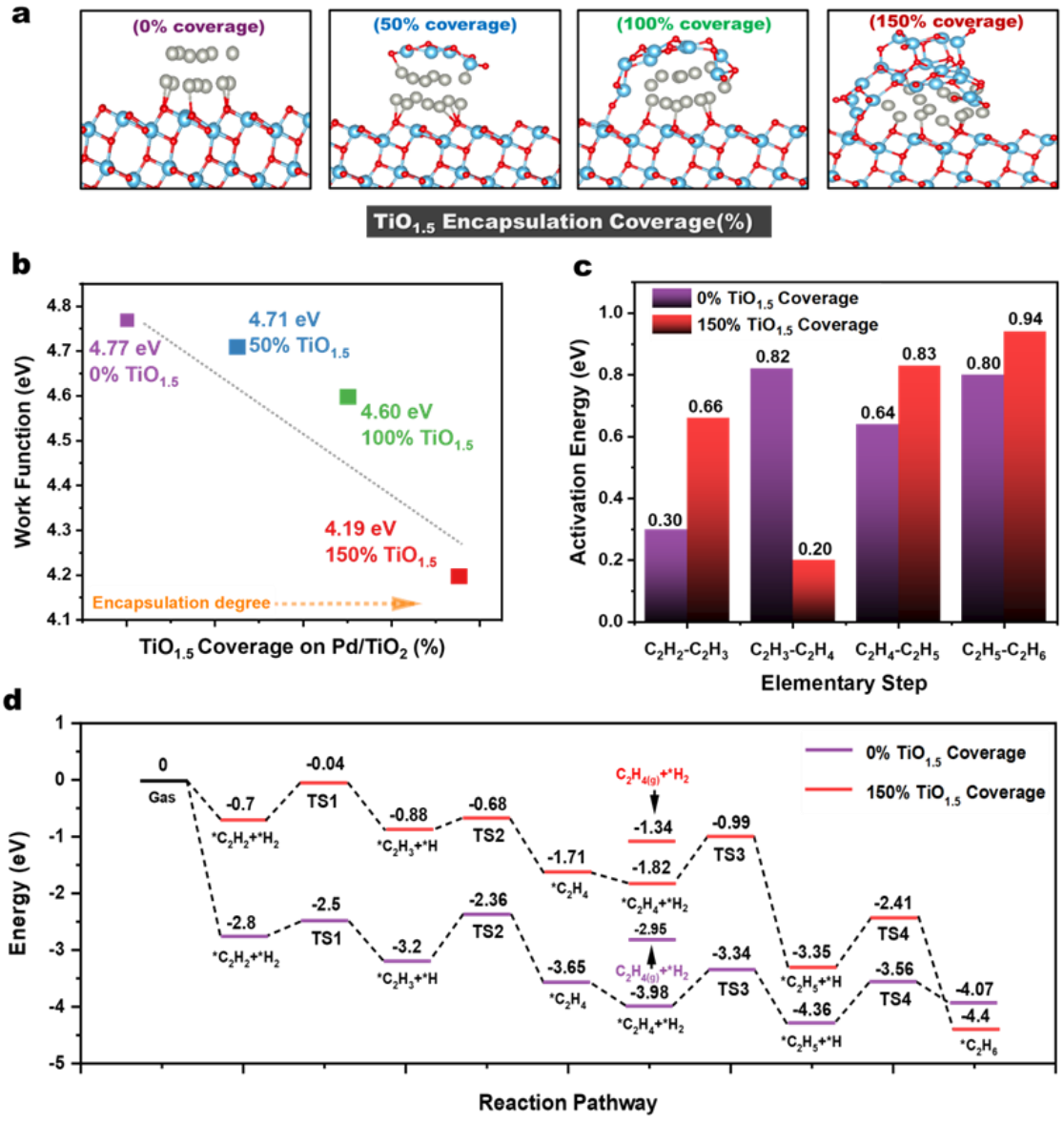

Figure 5 (a) Pd_{13} cluster models with varying TiO_x (x = 1.5) encapsulation (0%, 50%, 100%, 150%). Color code: Pd (grey), Ti (blue), O (red). (b) Calculated work functions of Pd/TiO_2 catalysts as a function of $TiO_{1.5}$ coverage. (c) E_a for acetylene hydrogenation steps on bare (0% encapsulation) and encapsulated Pd/TiO_2 (150% encapsulation). (d) Reaction energy profiles for acetylene hydrogenation.

Conclusion

In conclusion, we demonstrate a dual-stimuli strategy to precisely control SMSI construction via in situ Fermi level tuning in aqueous media. By combining ultrasonication with pH modulation, the Fermi level of supported metal catalysts is dynamically adjusted, enabling tunable overlayer encapsulation under ambient conditions. Lower pH drives stronger SMSI formation, enhancing oxygen vacancy formation and reduced Ti specie migration at the metal–support interface and results in superior activity and selectivity in both gas-phase and non-polar liquid-phase hydrogenation reactions. This approach provides a generalizable, low-temperature pathway to engineer electronic and geometric properties of heterogeneous catalysts, establishing a robust platform for sustained catalytic performance beyond conventional high-temperature SMSI strategies.

Acknowledgements

The research was supported financially by the U.S. Department of Energy (DOE), Office of Science, Office of Basic Energy Sciences, Chemical Sciences, Geosciences, and Biosciences Division, Catalysis Science program. Use of the NSLS-II (NIST beamline 6-BM and the 28-ID-1 beamline) was supported by the Department of Energy Office of Science User Facility operated for the DOE Office of Science by Brookhaven National Laboratory (BNL) under contract no. DE-SC0012704. Additionally, this research used resources of the Center for Functional Nanomaterials (CFN), which is a U.S. Department of Energy Office of Science User Facility, at Brookhaven National Laboratory under Contract No. DE-SC0012704. Work at ORNL's Spallation Neutron Source was sponsored by the Scientific User Facilities Division, Office of Basic Energy Sciences, U.S. Department of Energy. Oak Ridge National Laboratory is managed by UT-Battelle, LLC, for U.S. DOE under Contract No. DEAC05-00OR22725. The beam time was allocated to VISION (BL-16) on proposal number IPTS-36045. Stanford Synchrotron Radiation Lightsource, SLAC National Accelerator Laboratory, is supported by the U. S. Department of Energy, Office of Science, Office of Basic Energy Science under Contract No. DE-AC02-76SF00515. The authors thank Ritimukta Sarangi and Arun Asundi for the experimental support for the X-ray absorption spectroscopy measurements performed in this work.

Keywords: Interface Chemistry • Strong Metal-Support Interaction • pH tuning • Fermi Level • Ultrasonication

Reference

[1] L. Liu, A. Corma, *Chemical reviews* **2018**, *118*, 4981-5079.
[2] T. W. van Deelen, C. Hernández Mejía, K. P. de Jong, *Nature Catalysis* **2019**, *2*, 955-970.
[3] M. Cargnello, V. V. T. Doan-Nguyen, T. R. Gordon, R. E. Diaz, E. A. Stach, R. J. Gorte, P. Fornasiero, C. B. Murray, *Science* **2013**, *341*, 771-773.
[4] T. Zhou, X. Li, J. Zhao, L. Luo, Y. Wang, Z. Xiao, S. Hu, R. Wang, Z. Zhao, C. Liu, W. Wu, H. Li, Z. Zhang, L. Zhao, H. Yan, J. Zeng, *Nat Mater* **2025**.
[5] H. Chen, Z. Yang, X. Wang, F. Polo-Garzon, P. W. Halstenberg, T. Wang, X. Suo, S.-Z. Yang, H. M. Meyer III, Z. Wu, *Journal of the American Chemical Society* **2021**, *143*, 8521-8526.
[6] T. Wang, J. Hu, R. Ouyang, Y. Wang, Y. Huang, S. Hu, W.-X. Li, *Science* **2024**, *386*, 915-920.
[7] S. J. Tauster, S. C. Fung, R. T. K. Baker, J. A. Horsley, *Science* **1981**, *211*, 1121-1125.
[8] M. Li, T. Zhang, S.-Z. Yang, Y. Sun, J. Zhang, F. Polo-Garzon, K. M. Siniard, X. Yu, Z. Wu, D. M. Driscoll, *ACS Catalysis* **2023**, *13*, 6114-6125.
[9] J. Zhang, D. Zhu, J. Yan, C.-A. Wang, *Nature Communications* **2021**, *12*, 6665.
[10] G. Wu, Y. Liu, J. Wang, *Acc. Chem. Res.* **2023**, *56*, 911-923.
[11] K. M. Siniard, M. Li, S. Z. Yang, J. Zhang, F. Polo‐Garzon, Z. Wu, Z. Yang, S. Dai, *Angew. Chem. Int. Ed.* **2023**, *135*, e202214322.
[12] Y. Sun, Z. Yang, S. Dai, *J. Phys. Chem. Lett.* **2023**, *14*, 2364-2377.
[13] H. Wang, L. Wang, D. Lin, X. Feng, Y. Niu, B. Zhang, F.-S. Xiao, *Nature Catalysis* **2021**, *4*, 418-424.
[14] J. C. Matsubu, S. Zhang, L. DeRita, N. S. Marinkovic, J. G. Chen, G. W. Graham, X. Pan, P. Christopher, *Nat. Chem.* **2017**, *9*, 120-127.
[15] A. Beck, X. Huang, L. Artiglia, M. Zabilskiy, X. Wang, P. Rzepka, D. Palagin, M. G. Willinger, J. A. van Bokhoven, *Nat Commun* **2020**, *11*, 3220.
[16] J. Zhang, H. Wang, L. Wang, S. Ali, C. Wang, L. Wang, X. Meng, B. Li, D. S. Su, F.-S. Xiao, *Journal of the American Chemical Society* **2019**, *141*, 2975-2983.
[17] H. Chen, S.-Z. Yang, Z. Yang, W. Lin, H. Xu, Q. Wan, X. Suo, T. Wang, D.-e. Jiang, J. Fu, *ACS Central Science* **2020**, *6*, 1617-1627.
[18] Z. Ma, S. Brown, J. Y. Howe, S. H. Overbury, S. Dai, *J. Phys. Chem. C* **2008**, *112*, 9448-9457.
[19] R. J. Clarke, I. J. Nice, J. C. Hicks, *J. Am. Chem. Soc.* **2024**.
[20] J. Dong, Q. Fu, H. Li, J. Xiao, B. Yang, B. Zhang, Y. Bai, T. Song, R. Zhang, L. Gao, *Journal of the American Chemical Society* **2020**, *142*, 17167-17174.
[21] X. Shi, Z. Wen, Q. Gu, L. Jiao, H.-L. Jiang, H. Lv, H. Wang, J. Ding, M. P. Lyons, A. Chang, *Nature* **2025**, 1-8.
[22] M. Xu, M. Peng, H. Tang, W. Zhou, B. Qiao, D. Ma, *Journal of the American Chemical Society* **2024**, *146*, 2290-2307.
[23] Y. Guo, J. Liang, Y. Huang, J. Yang, Q. Zhang, A. Wang, B. Qiao, J. Li, T. Zhang, *Acc. Chem. Res.* **2025**, *58*, 2440-2453.

[24] T. S. Wesley, Y. Román-Leshkov, Y. Surendranath, *ACS Central Science* **2021**, *7*, 1045-1055.
[25] I. Ledezma-Yanez, W. D. Z. Wallace, P. Sebastián-Pascual, V. Climent, J. M. Feliu, M. Koper, *Nat. Energy* **2017**, *2*, 1-7.
[26] M. F. Toney, J. N. Howard, J. Richer, G. L. Borges, J. G. Gordon, O. R. Melroy, D. G. Wiesler, D. Yee, L. B. Sorensen, *Nature* **1994**, *368*, 444-446.
[27] T. Pu, W. Zhang, M. Zhu, *Angewandte Chemie International Edition* **2023**, *62*, e202212278.
[28] H. Zhao, Y. Zhu, H. Ye, Y. He, H. Li, Y. Sun, F. Yang, R. Wang, *Advanced Materials* **2023**, *35*, 2206911.
[29] T. Baidya, P. Bera, B. D. Mukri, S. K. Parida, O. Kröcher, M. Elsener, M. Hegde, *J. Catal.* **2013**, *303*, 117-129.
[30] X. Wang, H. Shi, J. H. Kwak, J. Szanyi, *ACS Catal.* **2015**, *5*, 6337-6349.
[31] Q. Wang, D. Tichit, F. Meunier, H. Guesmi, *J. Phys. Chem. C* **2020**, *124*, 9979-9989.
[32] F. C. Meunier, *J. Phys. Chem. C* **2021**, *125*, 21810-21823.
[33] H. Chen, Z. Yang, X. Wang, F. Polo-Garzon, P. W. Halstenberg, T. Wang, X. Suo, S.-Z. Yang, H. M. Meyer, Z. Wu, S. Dai, *J. Am. Chem. Soc.* **2021**, *143*, 8521-8526.
[34] P. Chen, A. Khetan, F. Yang, V. Migunov, P. Weide, S. P. Stürmer, P. Guo, K. Kähler, W. Xia, J. Mayer, *ACS Catal.* **2017**, *7*, 1197-1206.
[35] E. Kozyr, P. Paciok, K. Janssens, V. Lagostina, R. Pellegrini, O. Usoltsev, A. Skorynina, M. Chiesa, D. De Vos, E. Groppo, *Journal of Catalysis* **2025**, 116448.
[36] P. Wu, S. Tan, J. Moon, Z. Yan, V. Fung, N. Li, S.-Z. Yang, Y. Cheng, C. W. Abney, Z. Wu, *Nature communications* **2020**, *11*, 3042.
[37] F. Farges, G. E. Brown, J. Rehr, *Phys. Rev. B* **1997**, *56*, 1809.
[38] X. Chen, S. S. Mao, *Chem. Rev.* **2007**, *107*, 2891-2959.
[39] B. Cui, H. Wang, J. Han, Q. Ge, X. Zhu, *J. Catal.* **2022**, *413*, 880-890.
[40] T. Le Mercier, J.-M. Mariot, P. Parent, M.-F. Fontaine, C. Hague, M. Quarton, *Appl. Surf. Sci.* **1995**, *86*, 382-386.
[41] H. Chen, Z. Yang, X. Wang, F. Polo-Garzon, P. W. Halstenberg, T. Wang, X. Suo, S. Z. Yang, H. M. Meyer, 3rd, Z. Wu, S. Dai, *J Am Chem Soc* **2021**, *143*, 8521-8526.
[42] M. Li, T. Zhang, S.-Z. Yang, Y. Sun, J. Zhang, F. Polo-Garzon, K. M. Siniard, X. Yu, Z. Wu, D. M. Driscoll, A. S. Ivanov, H. Chen, Z. Yang, S. Dai, *ACS Catal* **2023**, *13*, 6114-6125.
[43] C. Di Valentin, G. Pacchioni, A. Selloni, *Phys. Rev. Lett.* **2006**, *97*, 166803.
[44] K. M. Siniard, M. Li, S. Z. Yang, J. Zhang, F. Polo-Garzon, Z. Wu, Z. Yang, S. Dai, *Angew Chem Int Ed* **2023**, *62*, e202214322.
[45] Q. Fu, T. Wagner, S. Olliges, H.-D. Carstanjen, *The Journal of Physical Chemistry B* **2005**, *109*, 944-951.
[46] Y. Li, Y. Zhang, K. Qian, W. Huang, *ACS Catalysis* **2022**, *12*, 1268-1287.
[47] K. Wang, T. Peng, Z. Wang, H. Wang, X. Chen, W. Dai, X. Fu, *Appl. Catal., B* **2019**, *250*, 89-98.
[48] S. F. Lee, E. Jimenez-Relinque, I. Martinez, M. Castellote, *Catalysts* **2023**, *13*, 1000.
[49] L. A. Lyon, J. T. Hupp, *The Journal of Physical Chemistry B* **1999**, *103*, 4623-4628.
[50] A. Imanishi, T. Okamura, N. Ohashi, R. Nakamura, Y. Nakato, *Journal of the American Chemical Society* **2007**, *129*, 11569-11578.
[51] P. Riesz, T. Kondo, C. M. Krishna, *Free Radical Research Communications* **1990**, *10*, 27-35.
[52] S. Merouani, O. Hamdaoui, F. Saoudi, M. Chiha, *Journal of Hazardous Materials* **2010**, *178*, 1007-1014.
[53] J. Li, Y. Lin, X. Pan, D. Miao, D. Ding, Y. Cui, J. Dong, X. Bao, *ACS Catal.* **2019**, *9*, 6342-6348.
[54] Z. Zhang, A. Nabera, G. Guillén-Gosálbez, J. Pérez-Ramírez, *Nature Chemical Engineering* **2025**, *2*, 99-109.
[55] J. Ballesteros-Soberanas, N. Martín, M. Bacic, E. Tiburcio, M. Mon, J. C. Hernández-Garrido, C. Marini, M. Boronat, J. Ferrando-Soria, D. Armentano, E. Pardo, A. Leyva-Pérez, *Nature Catalysis* **2024**.
[56] L. Zhang, M. Zhou, A. Wang, T. Zhang, *Chem. Rev.* **2020**, *120*, 683-733.
[57] F. Studt, F. Abild-Pedersen, T. Bligaard, R. Z. Sørensen, C. H. Christensen, J. K. Nørskov, *Science* **2008**, *320*, 1320-1322.
[58] J. H. Kang, E. W. Shin, W. J. Kim, J. D. Park, S. H. Moon, *Journal of catalysis* **2002**, *208*, 310-320.
[59] A. J. McCue, J. A. Anderson, *Frontiers of Chemical Science and Engineering* **2015**, *9*, 142-153.
[60] Z. Wang, F. Xie, J. Liu, X. Jian, Y. Wang, Y. Wang, C. Fan, R. Li, J. Wang, *Small* **2025**, 2503604.
[61] P. Weerachawanasak, O. Mekasuwandumrong, M. Arai, S.-I. Fujita, P. Praserthdam, J. Panpranot, *Journal of Catalysis* **2009**, *262*, 199-205.
[62] M. Xu, A. Zada, R. Yan, H. Li, N. Sun, Y. Qu, *Phys. Chem. Chem. Phys.* **2020**, *22*, 4526-4532.
[63] J. Moon, Y. Cheng, L. L. Daemen, M. Li, F. Polo-Garzon, A. J. Ramirez-Cuesta, Z. Wu, *ACS Catalysis* **2020**, *10*, 5278-5287.

Entry for the Table of Contents

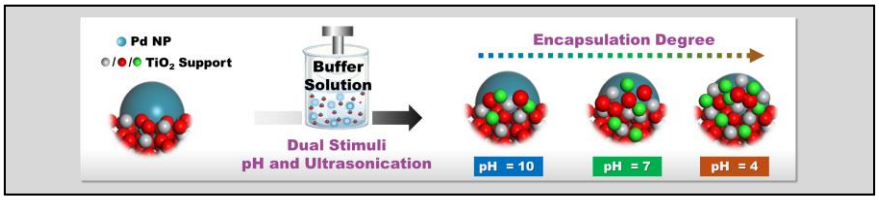

A dual-stimuli strategy was developed that couples pH adjustment with ultrasonication to construct strong metal-support interaction (SMSI) in aqueous media via dynamic Fermi-level regulation. In situ pH-induced charge redistribution at the metal–support boundary enables controlled encapsulation of metal nanoparticles. The resulting catalysts feature adjustable SMSI strength and exhibit improved activity and selectivity in hydrogenation.